

Microstructure, Hardness, and Wear Assessment of Spark-Plasma-Sintered Ti-xAl-1Mo Alloy



SAMSON OLAITAN JEJE, MXOLISI BRENDON SHONGWE,
ENOCH NIFISE OGUNMUYIWA, AZEEZ LAWAN ROMINIYI,
and PETER APATA OLUBAMBI

Alloys from the Ti-Al-Mo ternary system are of high importance in aerospace applications due to their excellent specific strength-to-density ratio, excellent corrosion, and creep resistance up to 600 °C. However, their sliding wear behavior has not been adequately explored. Cp-Ti and Ti-xAl-1Mo ($x = 3, 5, 7$) based near-alpha titanium alloys were successfully compacted by spark plasma sintering. The effect of Al addition on the densification, microhardness, and wear behavior of the developed alloys was studied. Results from the experiment showed that all compacts were almost fully densified. An increase in the value of the microhardness was recorded from 208 ± 10 to 352 ± 17 HV as the Al content increased. Al additions played an important role in the wear performance of the sintered alloy as detected from the coefficient of friction obtained with the sliding time and varying normal load. The alloyed Ti compacts had improved wear resistance. The wear rate values of alloyed compacts were 14 to 48.54 pct lower compared to the sintered Cp-Ti compacts tested as the Al content increased. The best wear resistance was observed for Ti-7Al-1Mo. Scanning electron microscopy micrographs, energy-dispersive spectroscopy, and wear debris show that the major wear mechanism detected was adhesive wear.

<https://doi.org/10.1007/s11661-020-05842-w>

© The Minerals, Metals & Materials Society and ASM International 2020

I. INTRODUCTION

FABRICATION of new and improvement of existing structural materials properties have been identified as the pertinent issue facing technological development and advancement globally. Technology is evolving rapidly, adapting to global industrial requirements such as the usage of structural materials in extreme conditions of which sliding wear is a major one. Titanium alloys are used widely in aerospace, shipbuilding, and chemical industries because of their unique properties, which entail high specific strength, excellent corrosion resistance, high thermal stability, and good mechanical

properties at elevated service temperature.^[1–5] However, the wider usage of these materials in applications that require sliding is restricted as a result of their poor wear resistance.^[6–12] This is attributed to the inability of titanium alloys to be highly resistive to plastic shearing and also to the low protection to surface oxide (formed as a result of frictional heating induced by high flash temperatures) during unlubricated sliding.^[13] High coefficient of friction (COF), low resistance to abrasion, and serious adhesive wear are the characteristics of the deficient tribological behavior of titanium alloy.^[7] There have been different proposed approaches by researchers to enhance the tribological properties of titanium alloys.

In recent years, alloying elements, such as α stabilizers (Al, O, C, N), neutral elements (Zr, Sn), or β stabilizers (Mo, V, Nb), or the combination of these (even in small percentages), have used with commercially pure titanium (Cp-Ti) to alter its microstructure, hence improving room-temperature mechanical properties.^[3,14,15] Among all variants of titanium alloys, near-alpha titanium alloy is the one candidate material that combines the α alloy excellent creep behavior with the $\alpha + \beta$ alloy high strength at temperatures above 400 °C.^[3,16] The Ti-Al-Mo system is characterized in that it has Al, regarded as the most important and widely used element, which can extend the α -phase field to a higher temperature, and also Mo, which is higher in

SAMSON OLAITAN JEJE, MXOLISI BRENDON SHONGWE, and AZEEZ LAWAN ROMINIYI are with the Institute for NanoEngineering Research, Department of Chemical, Metallurgical and Materials Engineering, Faculty of Engineering and Built Environment, Tshwane University of Technology, Pretoria 0001, South Africa. Contact e-mail: jejesamsonn@gmail.com ENOCH NIFISE OGUNMUYIWA is with the Department of Chemical, Materials and Metallurgical Engineering, Botswana International University of Science and Technology, Palapye, Botswana. PETER APATA OLUBAMBI is with the Centre for Nanoengineering and Tribocorrosion, School of Mining, Metallurgy and Chemical Engineering, University of Johannesburg, Johannesburg, South Africa.

Manuscript submitted January 14, 2020.

Article published online June 10, 2020

beta phase stabilizing capability than any other transition element.^[17] Mo atoms in α -Ti grains tend to enhance workability and improve the tribological behavior of Ti-based alloys while keeping their hardness at a very high level. Near-alpha contains a weight fraction of about 1 to 2 pct β stabilizers, which introduces the β phase of about 5 to 10 pct into the alloy at ambient temperature.^[3,15] There is the enablement of two-phase strengthening through alteration over the two phases' scale, structure, and arrangement due to the presence of the β phase; these made them largely used in the compressor section of aeroengines.

Spark plasma sintering (SPS) is usually used in the fabrication of complex geometry parts such as gears and structural parts. The technique entails synthesis and a process that makes bonding/sintering of metal powders possible at low sintering temperatures and a short time by the use of electrical energy to generate plasma and charge the spaces between powder particles, efficiently applying pressure at high temperature.^[18–20] SPS is preferred to conventional methods of powder metallurgy due to its operational ease, effective reproducibility, safety, short sintering time, and reliability.^[18,21] In the SPS technique, a spark is discharged at the gap between the powder particles, generating a local high-temperature state; this causes the powder particles' surface to evaporate and melt to transform into a fully dense composite. The possibility of consolidating micro- or nanopowders in SPS without excessive grain growth is attributed to the high rate of heating, short sintering time, and the temperatures involved.^[22]

Several kinds of research have been undertaken to study the wear mechanisms of titanium alloys. Obadele *et al.*^[23] investigated the wear behavior of Ti6Al4 V by the addition of ZrO₂ reinforcement under varying loads; it was established that ZrO₂ addition refines the microstructure and increases the hardness, reduces the friction coefficient, and enhances the Ti-6Al-4 V alloy wear resistance fabricated under the same condition. Molinari *et al.*^[24] studied the wear resistance of Ti-6Al-4 V using the disk-on-disk dry sliding tester, by varying the sliding speed and normal load conditions. They discussed that titanium alloys' poor wear resistance can be ascribed to the low resistance to plastic shear, low work hardening, and low protection provided by the surface oxide (produced by friction-induced high flash temperatures during the process of sliding). Chauhan and Dass^[25] investigated Ti-6Al-4 V alloy wear behavior under unlubricated sliding conditions and highlighted the mechanisms involved under varying applied normal force, sliding distance, and sliding speed setup. There was an increase in the specific wear rate as the normal applied force and speed increased and a specific wear rate decrease as the sliding distance increased or as the sliding speed decreased. Chowdhury *et al.*^[26] reiterated the fact that the mechanism of friction coefficient and wear rate is affected by several interfacial conditions: normal load, sliding speed, sliding distance, geometry, material type, temperature, relative surface motion, rubbing surfaces roughness, system rigidity, lubrication, humidity, stick-slip, and vibration.

Titanium alloys from the Ti-Al-X (where X is a β -Ti stabilizer) ternary system possess excellent mechanical properties and machinability combination and are mainly used in aerospace, biomedical, and petrochemical applications.^[27] However, most of the studies on wear have focussed more on Ti-6Al-4V, and there have been few or no reports on the wear behavior of alloys from the Ti-Al-Mo system against the alloy steel ball.^[25] Mo is a better β -Ti stabilizer, cheaper, and nontoxic element relative to V.^[27] Therefore, research in the development of alloys from the Ti-Al-Mo ternary system will broaden the application of titanium alloys in areas where wear resistance is of utmost priority. This study investigates the influence of applied normal load and Al addition on the microstructure, phase transformation, hardness, and dry sliding wear behavior of spark-plasma-sintered Ti-xAl-1Mo alloy.

II. MATERIALS AND METHODS

A. Materials and Sample Preparation

The starting materials used in the experiments were Cp-Ti, Al, and Mo powders, whose compositions are shown in Table I. Cp-Ti and Ti-xAl-1Mo ($x = 3, 5, 7$) samples were consolidated using the SPS machine (model HHPD-25 FCT type SPS equipment, Germany). The sintering was done in two stages. Stage 1 sintering was done at temperatures of 800 °C, 1000 °C, and 1100 °C to optimize the sintering temperature for Cp-Ti, while stage 2 sintering was done at the optimized temperature to sinter Cp-Ti and Ti-xAl-Mo compacts. All samples were sintered at a heating rate of 100 °C/min, pressure of 50 MPa, and holding time of 10 minutes under a vacuum condition of 10⁻² torr throughout the experiment. Before the sintering process, a plastic bottle containing up to 20 pct volume of Ti-xAl-Mo powder was subjected to mixing in a turbula mixer (WAB TURBULA SYSTEM SCHATZ) chamber at 49 rpm for 8 hours to achieve homogeneity of the mix. The scanning electron microscopy (SEM) micrograph and energy-dispersive spectroscopy (EDS) of the Ti-7Al-Mo powder mixture are shown in Figure 1 to confirm the even distribution of the mixed powders. Thereafter, Cp-Ti powder was loaded into a 20-mm inner diameter graphite die pressed at both ends with graphite punches, and the same was done for the admixed Ti-xAl-1Mo powder. After sintering, the specimen was left in the sintering machine to cool before removal at room temperature. Surface graphite contaminations were removed from the sintered compacts by sandblasting.

B. Sintered Sample Characterization

The densities of the compacts were obtained using Archimedes' principle. The relative densities were calculated by comparing the measured densities with the theoretical densities (using the rule of powder mixture) of the compacts. The specimens for the microhardness test were prepared using typical metallographic

Table I. Description of Elemental Powders

Sample	Particle Size (μm)	Purity (Pct)	Density (g/cm^3)	Melting Point ($^{\circ}\text{C}$)
Cp-Ti	1 to 25	99.8	4.5	1670
Al	1 to 25	99.5	2.7	660
Mo	2 to 4	99.9	10.28	2623

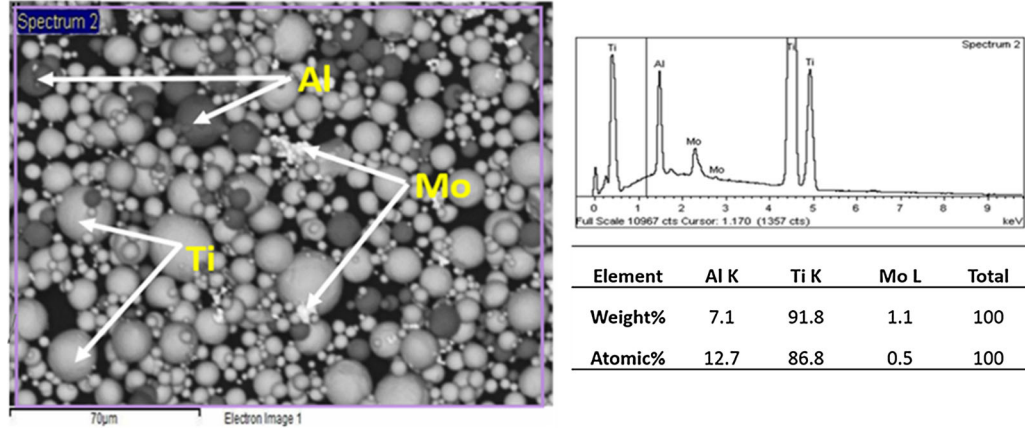


Fig. 1—SEM micrograph and EDS of Ti-7Al-1Mo admixed powders.

procedures for Ti alloys. A Vickers microhardness tester (FUTURE-TECH FM 800) was used for the microindentation test of the compacts' polished surface at room temperature using a load of 1 Kgf and dwell time of 15 seconds. The average result of 10 indentations on each sample was used as the hardness value of the sample.

C. Dry Sliding Wear Test

The tribology studies were carried out using a RTec universal tribometer (MFT-5000) with a reciprocating wear drive to compare different loads since load plays a major role in the wear properties of materials. An alloy steel grade ball with a diameter of 6.35 mm was used for counterface rubbing against the compacts. Varying loads of 15, 25, and 35 N were applied at a speed of 4 mm/s, length of 5 mm, for 600 seconds under unlubricated conditions at ambient temperature. Samples to be tested were secured inside the wear chamber and the alloy steel graded counterface ball was mounted on the steel ball holder of a suspension system. The reciprocating sliding friction test done on each sample at a particular set of conditions was repeated 3 times, and the wear volume calculated was based on the average value. The control of the load was made possible by a highly sensitive sensor, which also records the normal load (F) as time progresses. The wear track depth (d) and COF were also monitored and recorded from the tribometer setup. The wear test samples were prepared based on the ASTM G133-05(2010) specifications.^[28] At the inception of each test, the surfaces of the ball and sample were wiped with acetone to remove any possible

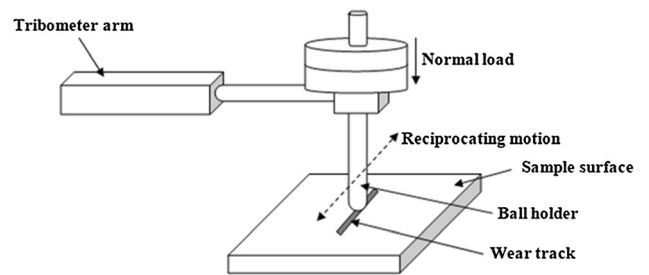


Fig. 2—Schematics of a reciprocating wear tester.

solid contaminants. The schematic diagram of a reciprocating wear tester is shown in Figure 2.

D. Microstructural Characterization of Wear Sample

The wear scar and debris were evaluated using a visible light microscope (for wear scar measurement) and an SEM (JEOL* JSM-7600F) equipped with EDS.

*JEOL is a trademark of Japan Electron Optics Ltd., Tokyo.

III. CALCULATION

A. Wear Volume and Rate

The wear scar length and width were measured using optical microscopy at the end of each test. Figure 3 shows two-dimensional (2-D) and three-dimensional (3-D) schematics representation of the wear track on the sample surface. The scar created by the wear is made

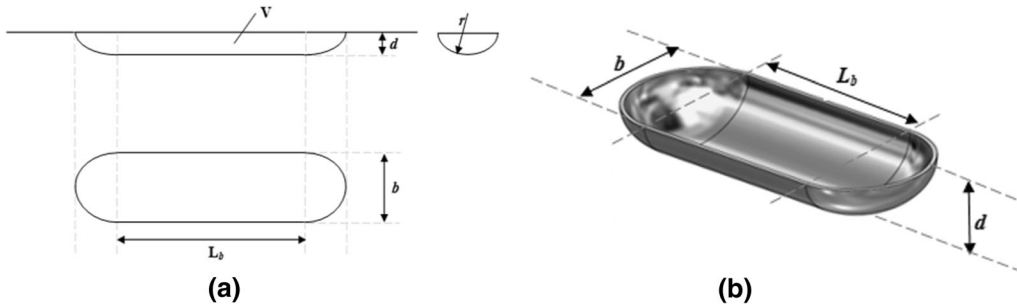


Fig. 3—(a) 2-D and (b) 3-D schematics wear scar created by a spherically tipped slider on a flat surface.

up of three sections, two portions of a spherical cut at the ends with radius r and a cylindrical surface cross section, b is the width, d is the depth, and L_b is the wear scar stroke length. The wear volume removed from the sample surface and the wear depth, d , can then be calculated using Eqs. [1] and [2], respectively, formulated by Qu and Truhan.^[29,30]

$$V = L_b \left[r^2 \arcsin\left(\frac{b}{2r}\right) - \frac{b(r-d)}{2} \right] + \frac{\pi}{3} d^2 (3r-d) \quad [1]$$

$$d = r - \sqrt{r^2 - \frac{b^2}{4}} \quad [2]$$

Equation [2] can be rewritten as Eq. [3]. Thus, the radius, r , was calculated from Eq. [3], since the wear scar width, b , is known from the optical measurement and the wear depth, d , is obtained from the tribology tester.

$$r = \frac{4d^2 + b^2}{8d} \quad [3]$$

The values of the wear volume loss were converted into wear rate, W_R , using Eq. [4], where V is the wear volume loss (mm^3), F is the applied normal load (N), and L is the total sliding distance (m).

$$W_R = \frac{V}{F \cdot L} \quad [4]$$

The total sliding distance is given in Eq. [5], where s is the reciprocating speed (mm/s) and t is total wear time (s):

$$L = s \cdot t \quad [5]$$

IV. RESULTS AND DISCUSSION

A. Sintering Temperature Optimization of Cp-Ti

Sintering of Cp-Ti was done at three different temperatures to determine the optimum temperature used to fabricate the developed alloy (Ti-xAl-1Mo). Figure 4 shows the XRD pattern of the sintered Cp-Ti samples at temperatures 800 °C, 1000 °C, and 1100 °C.

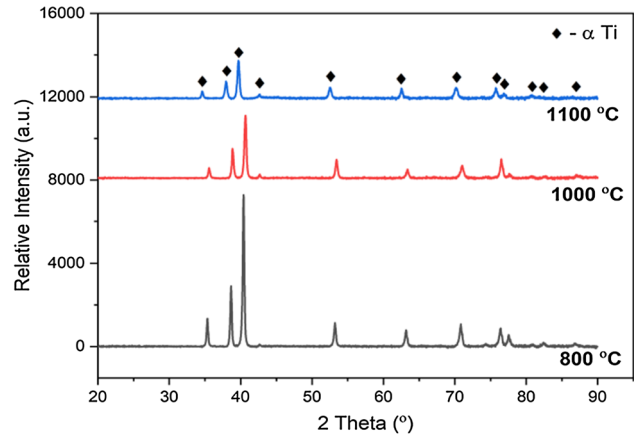


Fig. 4—X-ray diffraction patterns of sintered Cp-Ti.

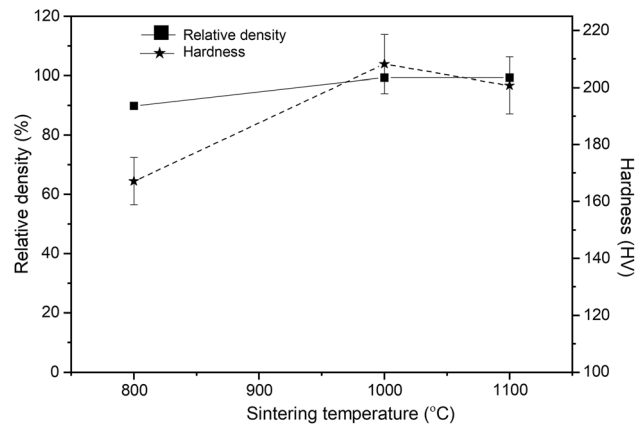


Fig. 5—Relative density and hardness behavior of Cp-Ti compacts.

Only peaks of α -Ti were observed for all the sintered samples, as Miklaszewski *et al.*^[31] and Shon *et al.*^[32] also reported.

Figure 5 shows the relative density graph and hardness of the Cp-Ti as a function of sintering temperature in the process of optimizing the sintering temperature of the Cp-Ti to be alloyed. It was observed that the compact sintered at temperature 800 °C has relatively high porosity with a relative density of 89.85 pct, which is responsible for the low value of hardness of 167 ± 8 HV. Compacts sintered at 1000 °C and 1100 °C were

fully densified, having a relative density of 99.36 and 99.28 pct, respectively. The increase in density implies there has been a decrease in porosity^[2,19]; this was confirmed from the SEM micrograph of the compacts as there were no visible pores. The sintering temperature increase leads to the increase in the energy available for particle deformation, rearrangement, and interparticle diffusion, hence eliminating the pores during the densification process, also justified elsewhere.^[32,33] This is in line with the study by Miklaszewski *et al.*,^[31] and it was indicated that the densification with temperature changes conforms to the Arrhenius equation in combination with the diffusion coefficient and that grain coarsening or migration of grain boundary might occur at higher sintering temperatures.

As seen in Table II, the microhardness value has a maximum of 208 ± 10 HV for the sample sintered at 1000 °C, which can be attributed to the high value of the relative density. This suggests that at the sintering temperature of 1000 °C, pressure of 50 MPa, heating rate of 100 °C/min, and holding time of 10 minutes, a fully densified sample of Cp-Ti can be sintered *via* SPS.

B. Microstructural Characterization of the Bulk Sample

Figure 6 shows the XRD pattern of the consolidated Cp-Ti and the reinforced Cp-Ti samples at a sintering temperature of 1000 °C. The XRD spectrum of the sintered Cp-Ti confirms only the presence of α -Ti, while all the alloyed Ti XRD spectra confirm the presence of α -Ti as the major phase with a small fraction transformed at the 2-theta angle of approximately 38.4 deg.

The presence of β -Ti in the reinforced Cp-Ti can be attributed to the fact that the sintering temperature might be above the β -transus temperature of the ternary alloy and also to the presence of Mo (a strong β stabilizer), which retained the β phase as the compacts cooled to ambient temperature. Small fractions of Mo_3Al_8 refractory phase were also detected. No titanium aluminide intermetallic was detected in any of the samples, which conforms with the Ti-Al phase diagram based on wt pct Al. Titanium aluminide (Ti_3Al) was detected in the study conducted by Jia *et al.*^[34] on alloys from the Ti-Al-Fe ternary system with just 5 wt pct Al at sintering temperature of 700 °C, which disappeared when the sintering temperature was raised to 1250 °C. The presence of Ti_3Al in their study can be attributed to the processing method (mechanical alloying of powders and reactive induction sintering) employed.

Table III shows the lattice parameters a , c , and V (unit cell volume) of the α -Ti matrix for each of the sintered compacts as obtained from X'pert HighScore

Plus software. There was a decrease in the lattice parameters a , c , and V but an increase in the ratio c/a as the concentration of Al increased in the sintered samples. This change (decrease) in the lattice parameters infers that the solid solution saturation limit has not been reached, as reported by Kornilov *et al.*^[35] The ratios c/a for the sintered compacts are lower compared to the 1.633 reported by Campbell^[36] for an ideal hexagonal structure. Higher values of the c/a ratio obtained for the alloy from the Ti-Al-Mo ternary system in comparison with the Cp-Ti could be attributed to the insertion of the Al and Mo interstitial atoms with a smaller atom radius.^[31]

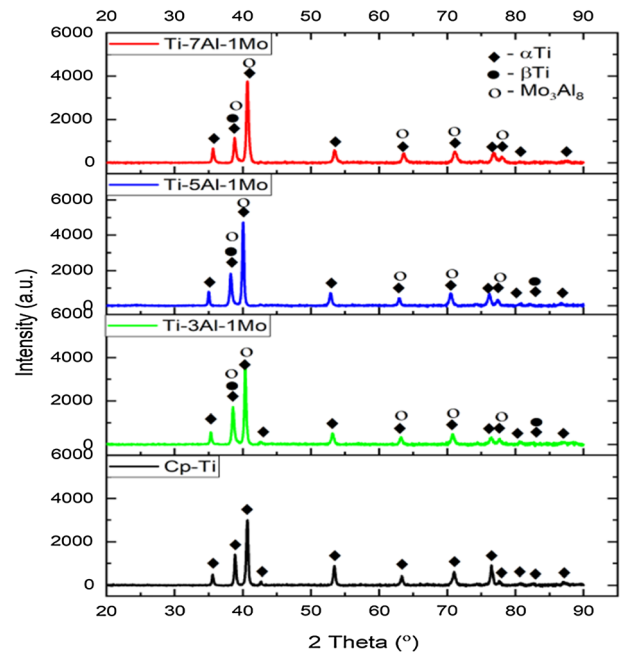


Fig. 6—X-ray diffraction patterns of sintered samples.

Table III. Sintered Sample Lattice Parameters of the Titanium Matrix

Sample	α -Ti Matrix Lattice Parameters			
	a (nm)	c (nm)	V (nm ³)	c/a
Cp-Ti	2.9505	4.6826	35.30	1.5871
Ti-3Al-1Mo	2.9511	4.6843	35.33	1.5873
Ti-5Al-1Mo	2.9440	4.6780	35.11	1.5890
Ti-7Al-1Mo	2.9200	4.6700	34.48	1.5993

Table II. Cp-Ti SPS Optimization Values at Different Sintering Temperatures

Sample	Sintering Temperature (°C)	Density (g/cm ³)	Relative Density (Pct)	Microhardness (HV)
Cp-Ti	800	4.049	89.85	167 ± 8
Cp-Ti	1000	4.477	99.36	208 ± 10
Cp-Ti	1100	4.496	99.28	201 ± 10

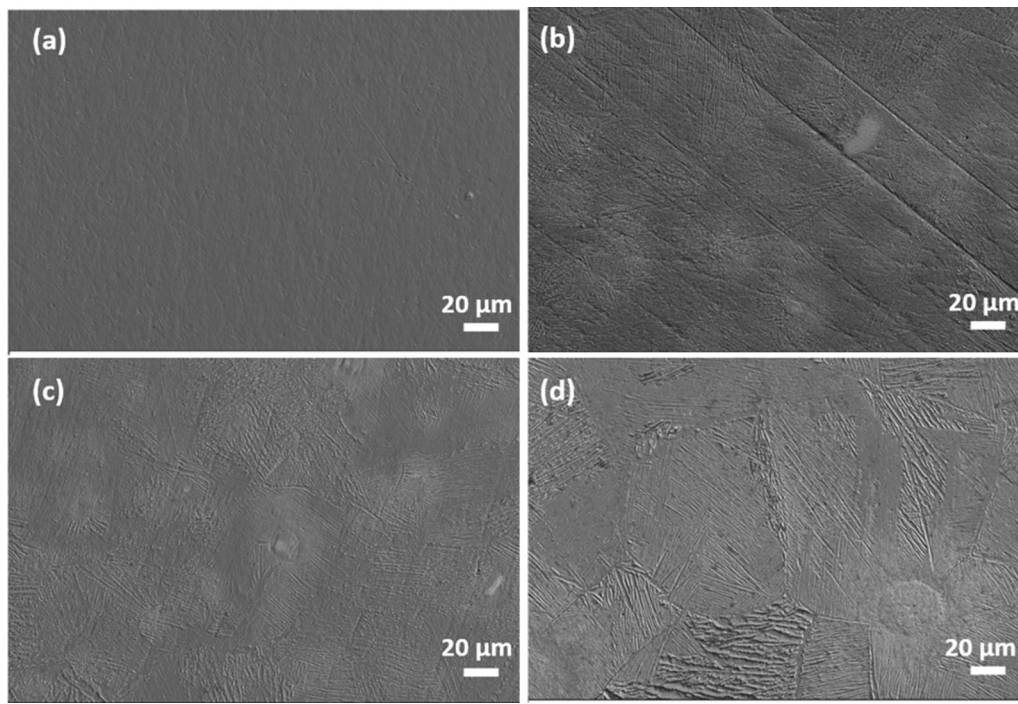


Fig. 7—SEM images of sintered samples at 1000 °C: (a) Cp-Ti, (b) Ti-3Al-1Mo, (c) Ti-5Al-1Mo, and (d) Ti-7Al-1Mo.

Figure 7 shows the microstructure of the SPS compacted Cp-Ti and Ti- x Al-1Mo ($x = 3, 5,$ and 7 wt pct) at sintering temperature of 1000 °C. Figure 7(a) denotes a typical micrograph of the as-sintered Cp-Ti with mostly α phase and no visible pores. Figures 7(b) through (d) denote the SEM micrographs of Ti-3Al-1Mo, Ti-5Al-1Mo, and Ti-7Al-1Mo ternary alloys, respectively, which are different from the micrograph of Cp-Ti. They comprise a nonporous microstructure with Mo-rich zone at some of the visible grain boundaries. The alloyed Cp-Ti shows a Widmanstätten lathlike morphology with major colonies of lamellar secondary alpha phase (α' phase) and minor fractions of mixed α and β phases at the grain boundaries. Al presence helps to stabilize the α phase, while Mo stabilizes the β phase.^[17] The micrographs of the alloys of the Ti-Al-Mo ternary system reported in this study are similar to the alloys of the laser deposited Ti-Al-V ternary system reported by Banerjee *et al.*^[37] The α -lath formation is more pronounced in Ti-7Al-1Mo; this can be attributed to the presence of the highest weight percent of Al, which stabilizes more of the α' phase.

C. Relative Density and Hardness

Table IV and Figure 8 illustrate the relative density and hardness of the sintered samples with varying weight fractions of Al at 1000 °C. It was observed that Al additions have little significance on the relative density of the compact, but they affect (enhance) the hardness of the sintered samples. All samples were fully densified, with Cp-Ti having a minimum of 99.36 pct.

The high value of the relative density observed can be attributed to the effect of liquid-phase sintering combined with the high uniaxial pressure and heating that SPS offers, which leads to Ti particles' neck formation and porosity annihilation, as also reported by Jeje *et al.*^[38] The microhardness value of Cp-Ti increased from 208 ± 10 to 290 ± 21 HV with the introduction of 3 wt pct Al and 1 wt pct Mo. There was no significant change in hardness value as the weight percentage of Al increased to 5 pct, but hardness increased significantly to 352 ± 25 HV with 7 wt pct Al. Al as a principal α stabilizer enhances the mechanical properties of Ti.^[3] This can also be attributed to the solid solution strengthening ability of Al in Ti. The increase in wt pct Al can increase the solute atom direct interaction with dislocation cores, which has been predicted by Kwasniak *et al.* as an α -Ti main strengthening mechanism.^[39]

D. Wear Behavior

The properties of the sintered Cp-Ti and Ti- x Al-1Mo compacts used for tribological investigations are summarized in Table IV. Cp-Ti sintered compact has the lowest relative density value of 99.36 pct. The microstructures of all sintered samples (Figure 7) reveal there were no pores that conform with the relative density values. The influence of pores on their tribological characteristics is, therefore, negligible. The wear test resulted in producing a scar that is, in all cases, visible to the naked eye, which implies that measurable wear was observed on all test samples.

Table IV. Density and Microhardness Properties of Cp-Ti and Ti-xAl-1Mo Compacts Sintered at 1000 °C

Sample	Sintering Temperature (°C)	Density (g/cm ³)	Relative Density (Pct)	Microhardness (HV)
Cp-Ti	1000	4.4770	99.36	208 ± 10
Ti-3Al-1Mo	1000	4.4394	99.95	290 ± 21
Ti-5Al-1Mo	1000	4.3798	99.9	290 ± 25
Ti-7Al-1Mo	1000	4.3700	99.68	352 ± 17

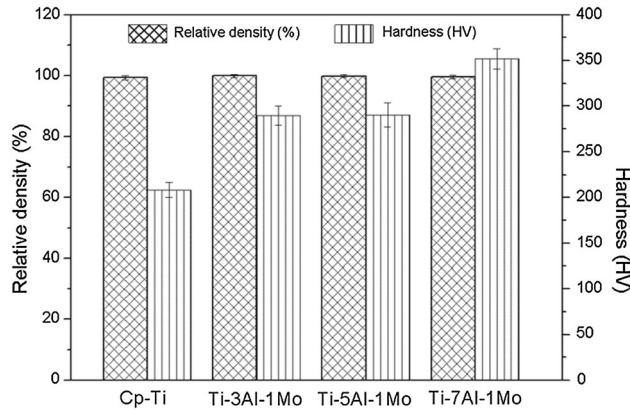


Fig. 8—Relative density and hardness behavior of SPS optimized Cp-Ti and Ti-xAl-1Mo compacts.

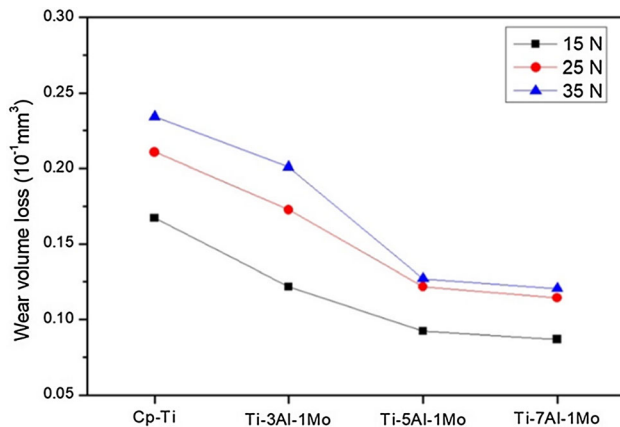


Fig. 9—Wear volume loss of sintered compacts as a function of composition and load.

1. Wear volume and wear rate

The wear volume loss variation in Cp-Ti and Ti-xAl-1Mo compacts subjected to varying applied normal loads is shown in Figure 9. It was seen that the wear volume loss increased as the load increased for all the tested compacts. This is in line with Eq. [4] and the fundamental laws of wear.^[40] However, the alloyed samples showed enhanced relative wear resistances over the unalloyed Cp-Ti compact as the weight fraction of Al increased from 3 to 7 pct. This can be attributed to the fact that the alloyed samples had higher microhardness values (Table II) and were not easily deformed under the applied loads.^[41,42] Zhang *et al.*'s^[43] study on

the wear behavior of Ti-6.5Al-3.5Mo-1.5Zr-0.3Si also follows the same pattern, whereby the wear rate of the sample decreases with increasing hardness value. This is in line with Archard's law,^[44] which states that wear volume loss of the material is inversely proportional to the material hardness value. This implies that the smaller volume loss is derived from materials with higher hardness value, as also stated by Liu *et al.*^[45]

It was observed that the wear volume loss followed the same trend for all applied loads (decreased) as the weight fraction of Al increased from 3 to 7 pct. This indicates that the addition of Al can enhance the wear resistance of Cp-Ti. This can be attributed to the α -Ti solid solution strengthening by Al, which is a result of mobile dislocation interaction with the Al atoms and dislocation density increment per strain as the Al atom increases.^[46] Generally, the least volume loss was observed in the alloy containing 7 wt pct Al.

The specific wear rate of samples decreases with increasing normal sliding load and also decreases with an increase in Al content. The wear rates of the unalloyed Cp-Ti sample were 4.64301×10^{-3} , 3.51078×10^{-3} , and $2.78888 \times 10^{-3} \text{ mm}^3/(\text{Nm})$ at a normal load of 15, 25, and 35 N, respectively. Also, the wear rates of the compacts with 7 wt pct Al were 2.56057×10^{-3} , 1.90477×10^{-3} , and $1.43514 \times 10^{-3} \text{ mm}^3/(\text{Nm})$ at a load of 15, 25, and 35 N, respectively, which is a decrease of about 45 to 49 pct. The decrease in specific wear rate as the load increases can be attributed to the fact that there is an increment in surface roughing, which might lead to the presence of hard oxidized wear debris ejected on the surface presenting itself as a metal (Ti and Al) oxide plateau (tribofilm) to decrease the friction.^[47] This was also observed in the study of Riyadh *et al.*^[48]

2. Frictional behavior

Figures 10(a) through (c) show a plot of a typical COF as a function of sliding time over a period of 600 seconds for all samples subjected to wear tests at loads of 15, 25, and 35 N, respectively. The plot shows that the alloyed Cp-Ti has a lower COF compared to the unalloyed Cp-Ti. However, at an applied load of 15 N, the highest stick amplitudes were observed for the COF profiles. The stick amplitudes reduced as the applied load increased, which suggests the prevalence of adhesive wear at low applied load. The plots show a similar pattern with the COF profile dropping as the Al content increases. The only variation observed was at 35 N normal load between 500 and 560 seconds sliding time for Cp-Ti, where the COF profile dropped drastically;

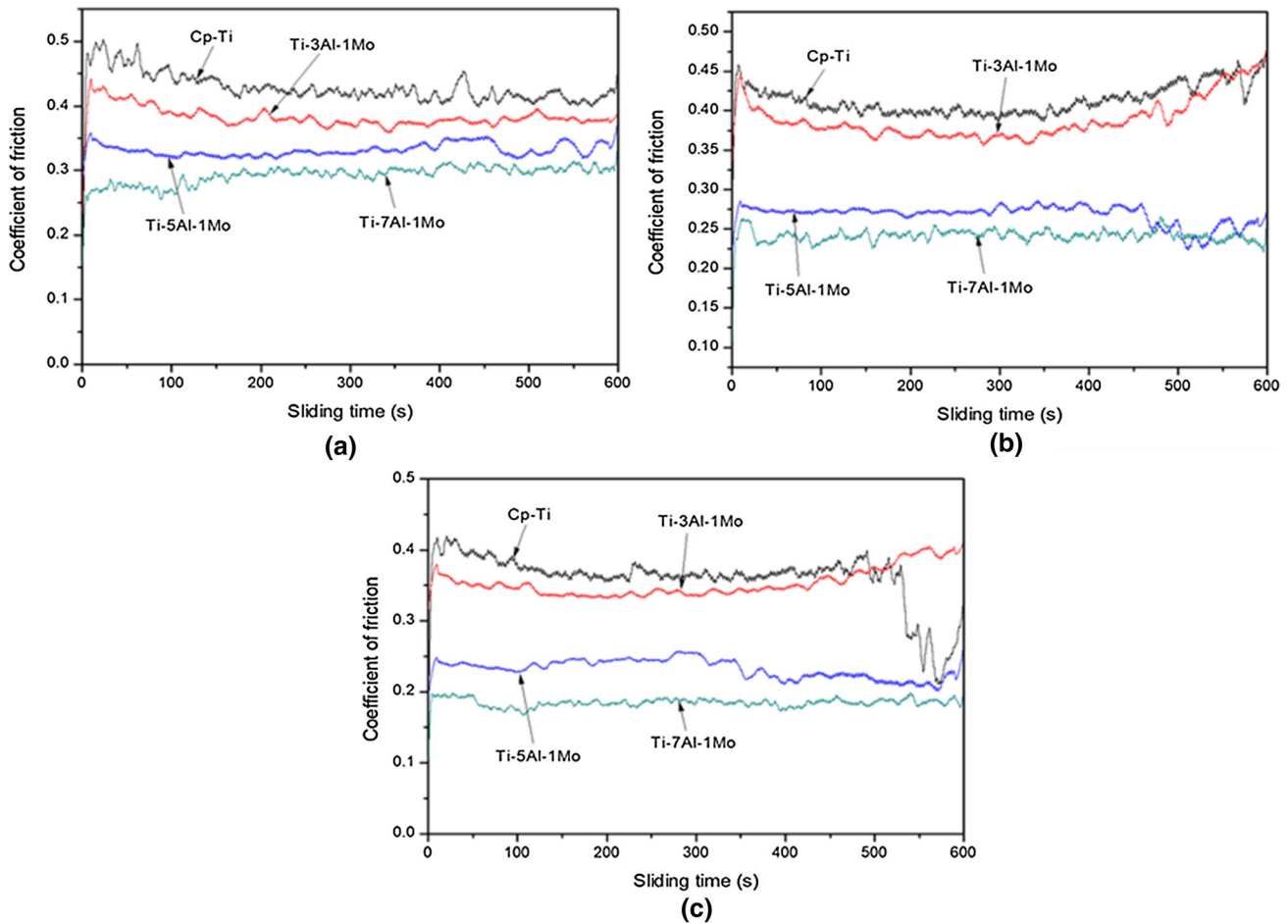


Fig. 10—COF variation of optimized Cp-Ti and Ti- x Al-1Mo under different applied loads: (a) 15 N, (b) 25 N, and (c) 35 N.

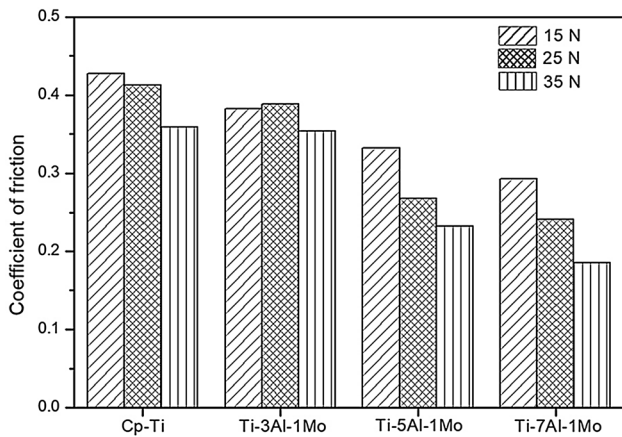


Fig. 11—Average COF values of sintered compacts as a function of composition and load.

this might be a result of a large accumulation of wear debris acting as a layer on the wear track.

Figure 11 shows the average steady-state COF values for the samples investigated at different normal loads. It (average steady-state COF) was found to decrease as the normal force increased for all the samples. The drop in COF as the normal load increased is in contrast to the

work of Zhong *et al.*^[49] on the Ti-20Zr-6.5Al-4 V alloy, and the authors suggested that when the normal load is increased, there is a sufficient increase in plastic strain to encourage delamination. However, this study is in line with that of Sharma and Sehgal,^[50] and they attributed the general drop in COF of Ti-6Al-4 V as the normal load increased to frictional heating and the alloy's low thermal conductivity. The drop in the average steady COF as the normal load increased in this study can be ascribed to the presence of hard oxidized Ti and Al wear debris.^[47] The mechanism can be related to a transformation from a two-body abrasion to a three-body abrasion, in which the wear debris act as abrasives between the alloyed steel ball and the wear track. These hard debris particles, which have the freedom to roll and also slide, are trapped in the grooves of the worn-out surface.^[47,51]

As observed, the COF dropped as the applied normal load was increased from 15 to 35 N for all samples. For each applied load, the compacts exhibited a lower COF in comparison to the Cp-Ti compact. Therefore, the frictional behavior of the observed samples indicates the strong effect of the Al addition in the compact composition. Among the observed alloyed samples, Ti-7Al-1Mo exhibited a minimum average COF of 0.1848.

3. Wear scar/debris morphology and wear depth

Figure 12 shows the SEM micrographs of the worn surfaces of the compacts tested at 15 and 35 N applied load. The micrographs of the worn-out surface at 25 N are not shown because they show characteristics that are in-between those of 15 and 35 N. There is evidence of abrasive wear, which is visible to the naked eye, on the worn surfaces of both unalloyed and alloyed Cp-Ti as the grooves created are in the same direction with the sliding direction of the worn-out surface.

At 15 N loads, the appearance of the initial formation of continuous plastically deformed grooves and delamination was seen on the compacts' wear tracks. This was found to be severe on the worn-out surface of the Cp-Ti compact at 35 N. Nonetheless, the degree of plastic deformation in the Ti-7Al-1Mo alloy is found to be smaller (Figures 12(d) and (h)). Samples with plastic deformations that are consistent are smoother at all tested loads. The presence of flakes produced by the delamination of material (Figures 12(b) and (c)) pointed

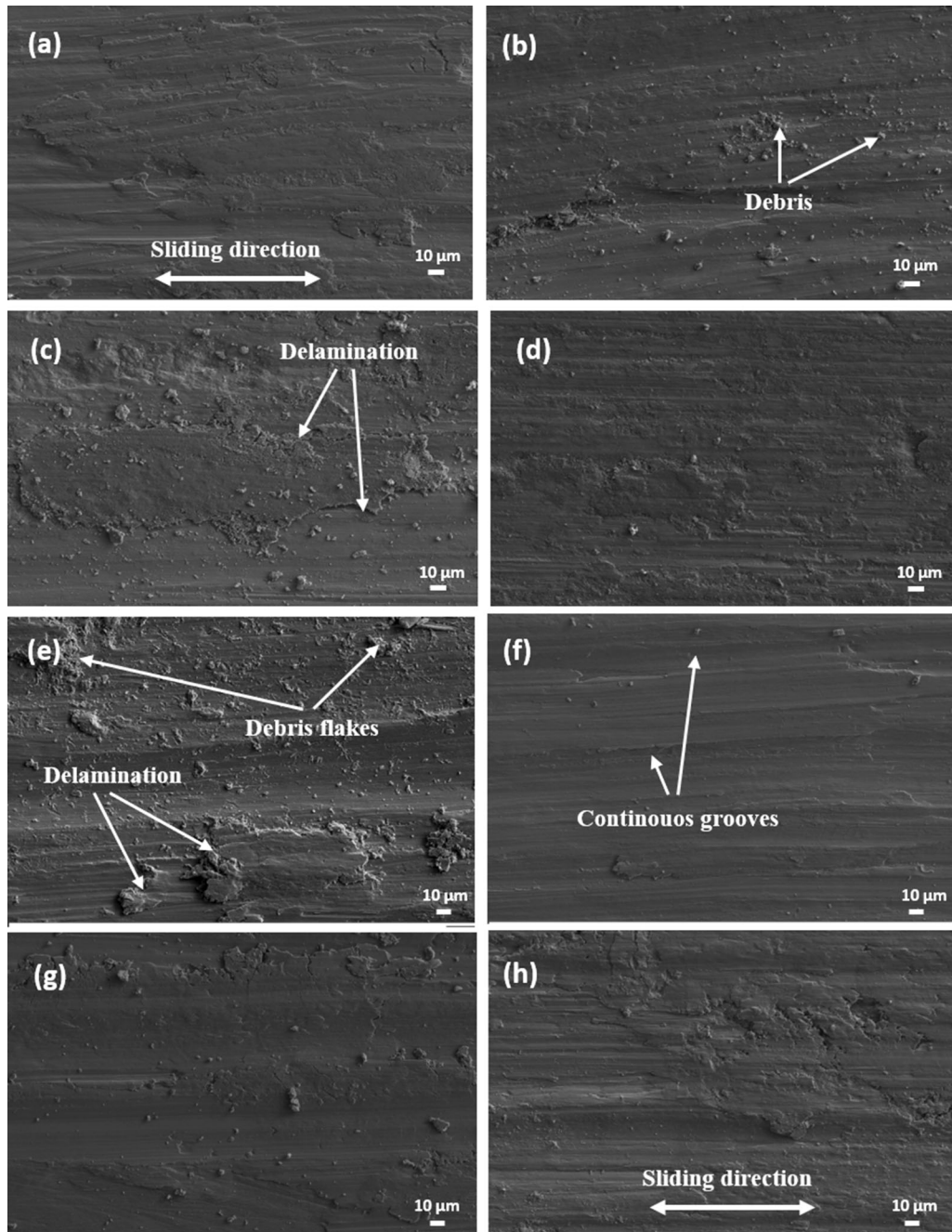


Fig. 12—SEM images of the worn surface of Cp-Ti, Ti-3Al-1Mo, Ti-5Al-1Mo, and Ti-7Al-1Mo, respectively, at loads of (a) through (d) 15 N and (e) through (h) 35 N.

out the existence of adhesive wear. Surface hardness is expected to affect the penetration depth. Therefore, since Ti-7Al-1Mo possesses the highest hardness value, the abrasion penetration of the surfaces is less. Thus, less material was removed by “plowing” action from the surface and less plastic flow was observed. Less flakelike chips on Ti-7Al-1Mo can be attributed to the adhesion strength contributed by the Al particles within the matrix of Ti, hence enhancing its plastic deformation resistance. These results are in agreement with the wear volume shown in Figure 9. The severity of adhesive wear could be observed by the flakelike wear debris sizes.^[52,53]

EDS spectra of the wear debris for Cp-Ti and Ti-7Al-1Mo are shown in Figure 13. Debris of Cp-Ti (Figure 13(a)) reveal the presence of Ti and O. Ti-7Al-1Mo debris (Figure 13(b)) reveal the major presence of Ti, Al, and O, then minor traces of Fe and C. This implies that the wear debris were primarily from the sintered compact and those from the counterface alloy steel ball were negligible. Also, oxidation of Ti took place at the surface of both compacts during wear. This established the fact that there was a possibility of metal oxide debris acting as a third body abrasion. Such tribo-oxide was also observed in the dry sliding wear study of Ti-6.5Al-3.5Mo-1.5Zr-0.3Si by Zhang *et al.*^[43]

The wear depths of Cp-Ti and Ti-7Al-1Mo with respect to the applied load after the dry sliding wear test are shown in Figure 14. It was observed in accordance with Archard’s law^[44] that the wear depth increased as

the applied load increased. Cp-Ti can be observed to exhibit higher wear depth that ranges from 50.52 to 59.57 μm relative to Ti-7Al-1Mo that ranges from 20.98 to 26.65 μm as the load increases from 15 to 35 N. This buttresses the fact that Ti-7Al-1Mo has a lower wear volume loss and wear rate. It was an expected result as the addition of Al and Mo to Cp-Ti brought about α -Ti

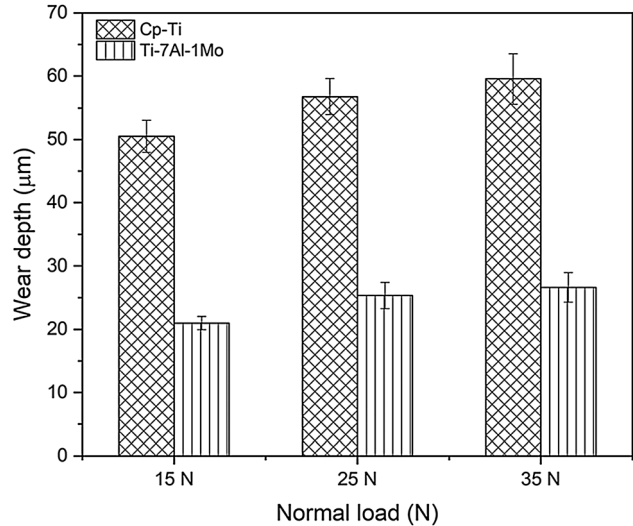


Fig. 14—Wear depth of Cp-Ti and Ti-7Al-1Mo under normal loads of 15, 25, and 35 N.

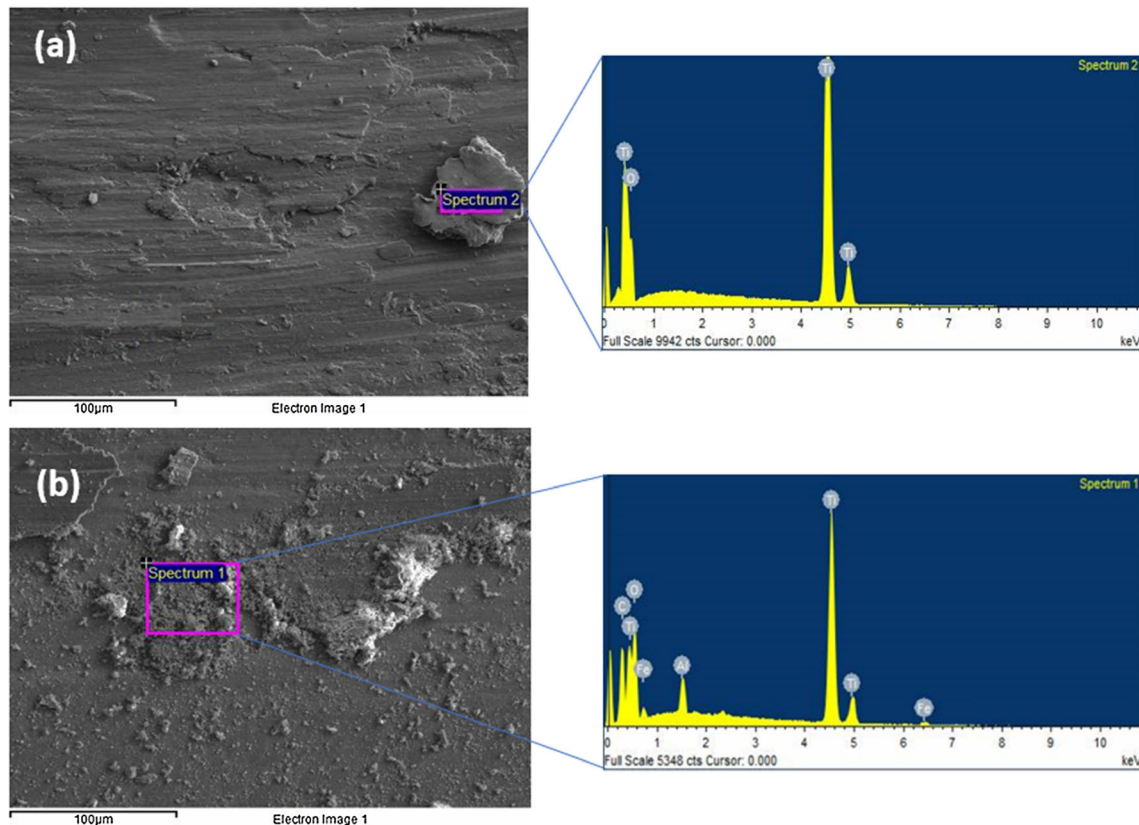


Fig. 13—SEM images and EDS of wear debris of (a) Cp-Ti and (b) Ti-7Al-1Mo under a test load of 35 N.

solid solution strengthening and also the formation of refractory Mo_3Al_8 intermetallic phase (as seen in Figure 6), which subsequently enhanced the microstructure and hardness of the Ti-7Al-1Mo alloy. In the study by Rominiyi *et al.*^[54] on the enhancement of the wear properties of Cp-Ti by varying wt pct Ni, it was also discovered that the formation of intermetallics was one of the reasons for the reduction in wear depth.

V. CONCLUSIONS

Unalloyed and alloyed Cp-Ti compacts were successfully fabricated by the SPS technique. The influence of Al on their density, microhardness, and dry sliding wear behavior was explored. The following deductions were drawn:

1. A fully densified sample of Cp-Ti can be sintered *via* SPS at the sintering temperature of 1000 °C, pressure of 50 MPa, heating rate of 100 °C/min, and holding time of 10 minutes.
2. All fabricated samples were fully densified with Cp-Ti having a minimum of 99.36 pct. The introduction of Al has little significance on the densification of the alloyed Cp-Ti.
3. The microhardness value of Cp-Ti increased with the introduction of Al and Mo. There was a significant increment in hardness value as the wt pct Al increased, with Ti-7Al-1Mo having the highest value of 352 ± 25 HV.
4. The wear volume loss increased with increasing applied load for all the tested samples, while the contrast was observed for the specific wear rate.
5. The alloyed samples (Ti-xAl-1Mo) show comparatively enhanced wear resistance over the unalloyed Cp-Ti compact as the weight fraction of Al increases from 3 to 7 pct. This was seen from the result of the wear volume and wear depth.

ACKNOWLEDGMENTS

This research was supported by National Research Foundation of South Africa Unique Grant No. 117867

REFERENCES

1. V.N. Chuvil'deev, V.I. Kopylov, A.V. Nokhrin, P.V. Tryaev, N.A. Kozlova, N.Y. Tabachkova, Y.G. Lopatin, A.V. Ershova, A.S. Mikhaylov, M.Y. Gryaznov, and M.K. Chegurov: *J. Alloys Compd.*, 2017, vol. 723, pp. 354–67.
2. O.E. Falodun, B.A. Obadele, S.R. Oke, M.E. Maja, and P.A. Olubambi: *J. Alloys Compd.*, 2018, vol. 736, pp. 202–10.
3. Y.M. Ahmed, K.S.M. Sahari, M. Ishak, and B.A. Khidhir: *Int. J. Sci. Res.*, 2014, vol. 3, pp. 1351–61.
4. M. Niinomi: in *Encyclopedia of Biomedical Engineering*, R. Narayan, ed., Elsevier, Oxford, United Kingdom, 2019, pp. 213–24.
5. F.A. Hajbagheri, S.K. Bozorg, and A. Amadeh: *J. Mater. Sci.*, 2008, vol. 43 (17), pp. 5720–27.
6. O.E. Falodun, B.A. Obadele, S.R. Oke, O.O. Ige, P.A. Olubambi, M.L. Lethabane, and S.W. Bhero: *Trans. Nonferrous Met. Soc. China*, 2018, vol. 28 (1), pp. 47–54.
7. L. Ceschini, E. Lanzoni, C. Martini, D. Prandstraller, and G. Sambogna: *Wear*, 2008, vol. 264 (1), pp. 86–95.
8. J. Ureña, E. Tabares, S. Tsipas, A. Jiménez-Morales, and E. Gordo: *J. Mech. Behav. Biomed. Mater.*, 2019, vol. 91, pp. 335–44.
9. G. Cassar, J.C.A.B. Wilson, S. Banfield, J. Housden, A. Matthews, and A. Leyland: *Wear*, 2010, vol. 269 (1), pp. 60–70.
10. A.W. El-Morsy: *Eng. Technol. Appl. Sci. Res.*, 2018, vol. 8 (1), pp. 2379–84.
11. Y. Qin, L. Geng, and D. Ni: *J. Mater. Sci.*, 2011, vol. 46 (14), pp. 4980–85.
12. X.X. Li, Y. Zhou, Y.X. Li, X.L. Ji, and S.Q. Wang: *Metall. Mater. Trans. A*, 2015, vol. 46A, pp. 4360–68.
13. S. Yerramareddy and S. Bahadur: *Wear*, 1991, vol. 142 (2), pp. 253–63.
14. W. Zhou, R. Sahara, and K. Tsuchiya: *J. Alloys Compd.*, 2017, vol. 727, pp. 579–95.
15. M. Textor, C. Sittig, V. Frauchiger, S. Tosatti, and D.M. Brunette: *Titanium in Medicine*, Springer, Berlin, 2001, pp. 171–230.
16. C. Leyens and M. Peters: *Titanium and Titanium Alloys: Fundamentals and Applications*, Wiley-VCH Verlag GmbH & Co. KGaA, Weinheim, Germany, 2003.
17. K. Hashimoto, M. Kimura, and R. Suyama: *Nippon Steel Technical Report*, Nippon Steel, Tokyo, 1994.
18. M.B. Shongwe, M.M. Ramakokovhu, S. Diouf, M.O. Durowoju, B.A. Obadele, R. Sule, M.L. Lethabane, and P.A. Olubambi: *J. Alloys Compd.*, 2016, vol. 678, pp. 241–48.
19. B.J. Babalola, M.B. Shongwe, B.A. Obadele, P.A. Olubambi, O.O. Ayodele, A.L. Rominiyi, and S.O. Jeje: *EDP Sciences MATEC Web of Conferences*, EDP Sciences, Les Ulis, France, 2018, vol. 249.
20. J. Guyon, A. Hazotte, J.P. Monchoux, and E. Bouzy: *Intermetallics*, 2013, vol. 34, pp. 94–100.
21. N. Weston, F. Derguti, A. Tudball, and M. Jackson: *J. Mater. Sci.*, 2015, vol. 50 (14), pp. 4860–78.
22. G. Suárez, Y. Sakka, T.S. Suzuki, T. Uchikoshi, X. Zhu, and E.F. Aglietti: *Sci. Technol. Adv. Mater.*, 2009, vol. 10 (2), p. 025004.
23. B.A. Obadele, A. Andrews, P.A. Olubambi, M. Mathew, and S. Pityana: *Wear*, 2015, vol. 328, pp. 295–300.
24. A. Molinari, G. Straffellini, B. Tesi, and T. Bacci: *Wear*, 1997, vol. 208 (1–2), pp. 105–12.
25. S.R. Chauhan and K. Dass: *Adv. Tribol.*, 2013, vol. 9, p. 324952.
26. M. Chowdhury, M. Khalil, D. Nuruzzaman, and M. Rahaman: *Int. J. Mech. Mechatron. Eng.*, 2011, vol. 11 (1), pp. 45–49.
27. F. Zhang, M. Yang, A.T. Clare, X. Lin, H. Tan, and Y. Chen: *J. Alloys Compd.*, 2017, vol. 727, pp. 821–31.
28. ASTM International: *Standard Test Method for Linearly Reciprocating Ball-on-Flat Sliding Wear. ASTM G133-05(2016)*, ASTM International, West Conshohocken, PA, 2016.
29. J. Qu and J.J. Truhan: *Wear*, 2006, vol. 261 (7), pp. 848–55.
30. S. Sharma, S. Sangal, and K. Mondal: *Wear*, 2013, vol. 300 (1), pp. 82–89.
31. A. Miklaszewski, D. Garbiec, and K. Niespodziana: *Adv. Powder Technol.*, 2018, vol. 29 (1), pp. 50–57.
32. J.H. Shon, J.M. Park, K.S. Cho, J.K. Hong, N.K. Park, and M.H. Oh: *Trans. Nonferrous Met. Soc. China*, 2014, vol. 24, pp. s59–s67.
33. H. Conrad: *MaterSci. Eng. A*, 2000, vol. 287 (2), pp. 227–37.
34. M.T. Jia, B. Gabbitas, and L. Bolzoni: *J. Mater. Process. Technol.*, 2018, vol. 255, pp. 611–20.
35. I. Kornilov, E. Pylaeva, and M. Volkova: *Russ. Chem. Bull.*, 1956, vol. 5 (7), pp. 787–95.
36. F.C. Campbell: *Elements of Metallurgy and Engineering Alloys, Metallic Structure*, ASM International, Materials Park, OH, 2008, p. 11.
37. R. Banerjee, D. Bhattacharyya, P.C. Collins, G.B. Viswanathan, and H.L. Fraser: *Acta Mater.*, 2004, vol. 52 (2), pp. 377–85.
38. S.O. Jeje, M.B. Shongwe, N. Makedi, A.L. Rominiyi, B.J. Babalola, and P.F. Lepele: *IOP Conf. Ser. Mater. Sci. Eng.*, 2019, vol. 655, p. 012018.

39. P. Kwasniak, H. Garbacz, and K. Kurzydowski: *Acta Mater.*, 2016, vol. 102, pp. 304–14.
40. Z. Wang, Y. Zhou, H. Wang, Y. Li, and W. Huang: *Mater. Lett.*, 2018, vol. 218, pp. 190–92.
41. X. Feng, J.H. Sui, W. Cai, and A.L. Liu: *Scr. Mater.*, 2011, vol. 64 (9), pp. 824–27.
42. G.D. Revankar, R. Shetty, S.S. Rao, and V.N. Gaitonde: *J. Mater. Res. Technol.*, 2017, vol. 6 (1), pp. 13–32.
43. Q. Zhang, H. Ding, G. Zhou, X. Guo, M. Zhang, N. Li, H. Wu, and M. Xia: *Metall. Mater. Trans. A*, 2019, vol. 50A, pp. 220–33.
44. I. Hutchings and P. Shipway: *Tribology: Friction and Wear of Engineering Materials*, Butterworth-Heinemann, Oxford, UK, 2017.
45. B. Liu, Y. Liu, X.Y. He, H.P. Tang, L.F. Chen, and B.Y. Huang: *Metall. Mater. Trans. A*, 2007, vol. 38A, pp. 2825–31.
46. H. Conrad and K.K. Wang: in *Strength of Metals and Alloys*, P. Haasen, V. Gerold, and G. Kostorz, eds., Pergamon Press, Oxford, United Kingdom, 1979, pp. 1067–72.
47. A. Abdelbary: in *Wear of Polymers and Composites*, A. Abdelbary, ed., Woodhead Publishing, Oxford, United Kingdom, 2014, pp. 37–66.
48. A. Riyadh, K. Rafezi, and A.D. Yarub: *J. Surf. Eng. Mater. Adv. Technol.*, 2012, vol. 2, pp. 167–173.
49. H. Zhong, L.Y. Dai, Y.J. Yang, Y. Yue, B.A. Wang, X.Y. Zhang, M.Z. Ma, and R.P. Liu: *Metall. Mater. Trans. A*, 2017, vol. 48A, pp. 5678–87.
50. M.D. Sharma and R. Sehgal: *Tribol Online*, 2012, vol. 7 (2), pp. 87–95.
51. T.S.N. Sankara Narayanan: in *Corrosion Protection and Control Using Nanomaterials*, V.S. Saji and R. Cook, eds., Woodhead Publishing, Oxford, United Kingdom, 2012, pp. 167–212.
52. J. Majumdar and I. Manna: *Metall. Mater. Trans. A*, 2012, vol. 43A, pp. 3786–96.
53. W. Hong, W. Cai, and S. Wang: *Chin. J. Aeronaut.*, 2018, vol. 31 (5), pp. 867–82.
54. A.L. Rominiyi, M.B. Shongwe, E.N. Ogunmuyiwa, B.J. Babalola, P.F. Lepele, and P.A. Olubambi: *Mater. Chem. Phys.*, 2020, vol. 240, p. 122130.

Publisher's Note Springer Nature remains neutral with regard to jurisdictional claims in published maps and institutional affiliations.